



Cite this: *J. Mater. Chem. B*, 2025, 13, 10576

A dual-targeting photosensitizer for simultaneous mitochondrial and lysosomal disruption in cancer and antibacterial photodynamic therapy†

Chaewoon Cho,^{a,c} K. M. K. Swamy,^a Bingqing Sun,^b Gyoungmi Kim,^a Lei Liu,^b *^b
 Won Jun Jang ^a and Juyoung Yoon *^{a,c}

Mitochondria and lysosomes are key organelles involved in cell survival and death. Mitochondria regulate energy production, reactive oxygen species (ROS) levels, and apoptosis, while lysosomes manage waste degradation and also play a role in cell death through enzyme release when damaged. Cancer cells often contain more active lysosomal enzymes, making them more vulnerable to lysosome-related cell death. Targeting these organelles with photosensitizers (PSs) in photodynamic therapy (PDT) can achieve enhanced anticancer effects. Dual-targeting PSs, especially those that affect both mitochondria and lysosomes, are rare but highly promising. By simultaneously damaging both organelles, such PSs may trigger stronger therapeutic responses. In this study, we present a novel dual-targeting photosensitizer, **MCQ-1**, which localizes to both mitochondria and lysosomes and serves as an efficient type I PS for cancer cell treatment. Additionally, **MCQ-1** demonstrates remarkable antibacterial activity against Gram-positive bacteria, including *Staphylococcus aureus* (*S. aureus*) and methicillin-resistant *S. aureus* (MRSA), under white LED irradiation.

Received 5th June 2025,
 Accepted 23rd July 2025

DOI: 10.1039/d5tb01345c

rsc.li/materials-b

Introduction

Photodynamic therapy (PDT) has emerged as a promising non-invasive therapeutic strategy, which employs photoactivatable agents to selectively eliminate pathological cells.¹ PDT utilizes photosensitizers (PSs) that, upon irradiation with light of an appropriate wavelength, generate reactive oxygen species (ROS), thereby inducing oxidative damage and subsequent apoptosis or necrosis in target cells.^{2–7} This strategy has demonstrated substantial potential in the treatment of malignant tumors and infectious diseases, owing to its spatiotemporal controllability, minimal invasiveness, and ability to overcome multidrug resistance.^{2–7}

The development of organelle-specific phototherapeutic agents has emerged as a critical priority for enhancing the selectivity and efficacy of cancer treatment.⁸ Mitochondria, as key regulators of bioenergetics, redox balance, and apoptotic pathways, represent highly attractive subcellular targets.^{9–14}

Recent insights into organelle crosstalk have underscored the functional interplay between mitochondria and lysosomes, which cooperatively regulate key metabolic pathways, such as lipid catabolism and glucose homeostasis, *via* lysosomal hydrolases.^{15–17} This bidirectional regulatory mechanism offers a compelling rationale for dual-organelle targeting. By concurrently disrupting lysosomal integrity (thereby impairing autophagic flux and lysosome-dependent mitochondrial quality control) and inducing mitochondrial dysfunctions, dual-targeting strategies potentiate oxidative stress and induce an energy crisis within cancer cells, significantly improving therapeutic outcomes. Nonetheless, only a few examples of mitochondria and lysosome dual-targeting systems have been reported to date.^{18–21}

On the other hand, bacterial and fungal infections remain a major global health concern, often leading to high mortality rates. Pathogenic bacteria are linked to various diseases, including skin infections, sepsis, and bacteremia, and may even cause cancer through chronic inflammation or the release of carcinogenic metabolites.²² The global rise of antibiotic resistance, driven by the overuse and misuse of antibiotics, has exacerbated this issue, leading to multidrug-resistant “superbugs.” These pathogens are now responsible for over 700 000 deaths annually.^{23,24} The growing threat of resistant bacteria highlights the urgent need for novel antimicrobial therapies that can overcome the limitations of conventional antibiotics.

^a Department of Chemistry and Nanoscience, Ewha Womans University, Seoul 03760, Korea. E-mail: jyo@ewha.ac.kr

^b College of Resource and Environment, Anhui Science and Technology University, Fengyang 233100, China. E-mail: liulei@feipan.org

^c Graduate Program in Innovative Biomaterials Convergence, Ewha Womans University, Seoul 03760, Korea

† Electronic supplementary information (ESI) available. See DOI: <https://doi.org/10.1039/d5tb01345c>



PDT has recently emerged as a promising alternative for combating microbial infections.^{25–29} Upon light activation, PSs produce ROS that effectively inactivate bacteria. PDT offers advantages such as flexible dosing and repeatability, making it an attractive strategy for antimicrobial treatment. Although traditionally applied in oncology and dermatology, this approach is now being explored for the treatment of infectious diseases. However, key challenges, such as optimizing the PS efficacy and targeting, must be addressed to fully realize its therapeutic potential against pathogens.

Herein, we report a new PS, **MCQ-1**, which localizes to both mitochondria and lysosomes and serves as an efficient type I PS for cancer cell treatment. Additionally, **MCQ-1** demonstrates remarkable antibacterial activity against Gram-positive bacteria, including *Staphylococcus aureus* (*S. aureus*) and methicillin-resistant *S. aureus* (MRSA), under white LED irradiation.

Results and discussion

Design and synthesis of MCQ-1

For the synthesis of **MCQ-1**, 9-(4-morpholinobutyl)-9*H*-carbazole-3-carbaldehyde (**2**) was first prepared following a previously reported procedure.^{30–32} Further reaction of **2** with 1,4-dimethylquinolin-1-ium iodide in the presence of piperidine afforded **MCQ-1** in 50.7% yield (Scheme 1). **MCQ-1** was fully characterized using ¹H and ¹³C NMR spectroscopy as well as high-resolution mass spectroscopy (ESI-HRMS) (Fig. S1–S5, ESI[†]). **MCQ-1** exhibited a donor–acceptor (D–A) structure, with carbazole as the electron donor and quinolinium iodide as the electron acceptor, leading to strong intramolecular charge transfer (ICT); this structure resulted in intense fluorescence and facilitated ROS generation. Additionally, its positive charge and the presence of morpholine enabled dual-targeting of mitochondria and lysosomes.

Photophysical properties of MCQ-1

First, to investigate the photophysical properties of **MCQ-1**, UV-vis absorption and fluorescence spectra were obtained in various solvents (Fig. 1A and B). In an ACN/PBS solution (5 : 95, v/v), **MCQ-1** showed the highest absorption peak at

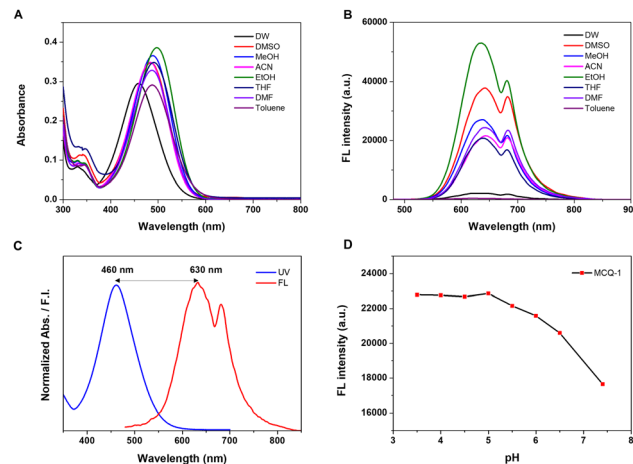


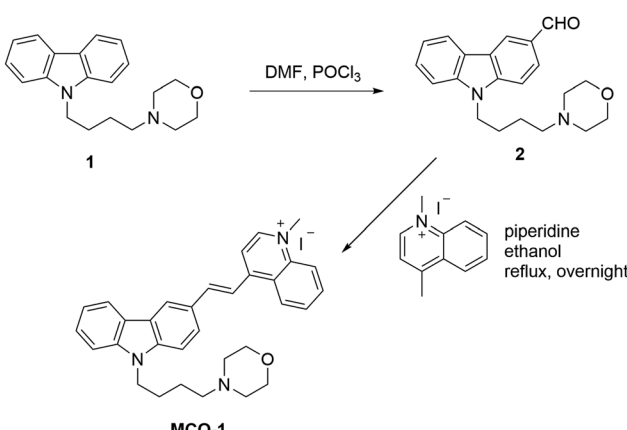
Fig. 1 (A) UV-vis absorption and (B) fluorescence spectra of **MCQ-1** (10 μ M) in different solvents; $\lambda_{\text{ex}} = 460$ nm. (C) Normalized absorption and emission spectra of **MCQ-1** (10 μ M) in ACN/PBS solution (5 : 95, v/v). (D) Fluorescence spectra of **MCQ-1** (10 μ M) at different pH values; the inset shows the corresponding intensities at 630 nm.

460 nm and displayed strong red fluorescence in the 600–700 nm region, with the maximum fluorescence emission observed at 630 nm (Fig. 1C). The large Stokes shift (170 nm) of **MCQ-1**, with a wide gap between the excitation and emission peaks, reduces self-absorption, making this PS highly suitable for fluorescence imaging.

Next, we examined the fluorescence spectra of **MCQ-1** under various pH conditions. Strong fluorescence was observed under acidic conditions (pH 3.5–5.0), but the fluorescence decreased as the pH increased from 5.5 to 7.4 (Fig. 1D). This is attributed to the photoinduced electron transfer (PET) effect from the nitrogen atom in the morpholine structure. However, no significant fluorescence quenching was observed at pH 7.4, indicating that **MCQ-1** can serve as a fluorescent probe in biological environments. On the other hand, under acidic conditions, the nitrogen atom in the morpholine structure, which possesses a lone pair of electrons, is readily protonated. This protonation suppresses the PET process, resulting in strong fluorescence.³⁹

ROS generation of MCQ-1

To investigate the photodynamic effect of **MCQ-1**, we examined its ROS generation ability. First, to evaluate the total ROS generation, fluorescence spectra were measured at different light irradiation times, using 2',7'-dichlorofluorescein diacetate (DCFH-DA) as the indicator. **MCQ-1** (10 μ M) in PBS buffer solution was irradiated with white LED light (50 mW cm^{-2}) for 10 s each time, from 0 to 90 s. The fluorescence peak intensity of DCFH-DA at 520 nm increased with increasing irradiation time (Fig. S6A and B, ESI[†]). This confirmed the ROS generation of **MCQ-1** when activated by light irradiation. Additionally, hydroxyphenyl fluorescein (HPF) was used under the same experimental conditions to detect the hydroxyl radical ($\cdot\text{OH}$) generation. As a result, the fluorescence peak of HPF at 512 nm increased with increasing irradiation time (Fig. S6C and D, ESI[†]), indicating that **MCQ-1** generates $\cdot\text{OH}$ upon light



Scheme 1 Synthesis of **MCQ-1**.



exposure. Solutions containing only DCFH-DA and HPF were used as controls, and neither showed a fluorescence increase under light irradiation. In contrast, no significant fluorescence changes were observed when ABDA and DHE were used to detect singlet oxygen (${}^1\text{O}_2$) and a superoxide radical anion ($\text{O}_2^{\bullet-}$), respectively, under the same conditions, indicating that **MCQ-1** does not generate ${}^1\text{O}_2$ or $\text{O}_2^{\bullet-}$ upon light irradiation (Fig. S7, ESI[†]). These experiments confirmed that **MCQ-1** acts as a PS capable of generating ROS through a type I mechanism, potentially causing the death of cancer cells or bacteria.

Theoretical calculations

The type I PS behavior of **MCQ-1** was further elucidated using density functional theory (DFT) and time-dependent density functional theory (TDDFT) calculations. Fig. 2A and B indicate that the HOMO and LUMO are well-separated spatially, indicating that the sensor exhibits ICT characteristics during the $\text{S}_0 \rightarrow \text{S}_1$ excitation. The electron–hole distribution was then analyzed, as shown in Fig. 2C and D. An equivalent of 0.37 electrons transfers from the carbazole to the quinolone moiety, with a separation distance of 5.37 Å. This denotes a very strong ICT, in terms of both the transfer number and the transfer distance. According to Tang *et al.*'s theory,^{33,34} a strong ICT will boost the ROS production by minimizing the energy difference between singlet and triplet states (ΔE_{ST}), which improves the triplet excited state yield. The calculated energy differences between the singlet and triplet states of **MCQ-1** are shown in Fig. 2E (Table S1, ESI[†]). As expected, the ΔE_{S1T2} value is only 0.15 eV, which is likely to facilitate the singlet/triplet ISC process and make **MCQ-1** a type I PS.

In vitro PDT effect

Next, the biocompatibility and PDT effect of **MCQ-1** were evaluated *in vitro* using the methyl thiazolyl tetrazolium (MTT) assay in HeLa cells. Under dark conditions, **MCQ-1** exhibited low cytotoxicity, maintaining a cell viability greater than 90% even at a concentration of 15 μM. In contrast, under light irradiation, the cell viability decreased sharply with increasing **MCQ-1** concentration (Fig. 3). During the same 10-min white LED irradiation treatment, a higher light intensity (0.5 W cm⁻²) resulted in a greater cancer cell death rate compared to that observed at 0.3 W cm⁻², indicating that stronger light led to

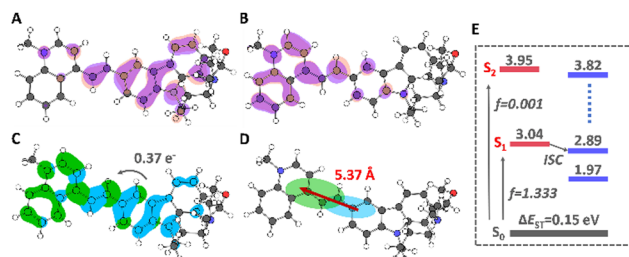


Fig. 2 (A) HOMO; (B) LUMO; (C) electron–hole distribution for the $\text{S}_0 \rightarrow \text{S}_1$ excitation process; (D) electron–hole separation; (E) energy level distribution of singlet and triplet states. Green and cyan surfaces represent electron and hole distributions, respectively; f represents the oscillator strength for the excitation process.

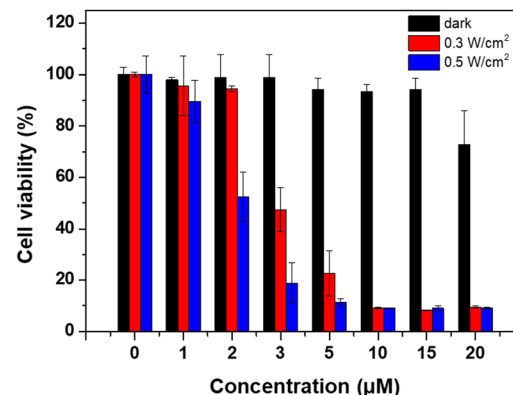


Fig. 3 Cell viability of HeLa cells after **MCQ-1** (1–20 μM) treatment with and without white LED irradiation (0.3, 0.5 W cm⁻², 10 min).

enhanced phototoxicity. Overall, these results confirmed that **MCQ-1** exhibits high biocompatibility in the dark along with strong PDT efficiency under light irradiation, demonstrating its potential as an effective PS for cancer treatment.

Mitochondria and lysosome staining

To confirm the dual-targeting ability of **MCQ-1** toward mitochondria and lysosomes, colocalization experiments were conducted using MitoTracker Blue and Lysotracker Deep Red as fluorescent probes. Colocalization fluorescence images were obtained using confocal laser scanning microscopy (CLSM). HeLa cells were co-stained with **MCQ-1** (5 μM, 30 min) and MitoTracker Blue (0.5 μM, 10 min); this was followed by CLSM imaging, which revealed clear colocalization, with a Pearson correlation coefficient (PCC) of 0.84 (Fig. 4A). Similarly, colocalization experiments with Lysotracker Deep Red showed a high PCC value of 0.95 (Fig. 4B). These results confirmed that **MCQ-1** enables the simultaneous imaging of mitochondria and lysosomes in live cancer cells.

In vitro fluorescence imaging and antibacterial tests

PDT is also considered a promising antimicrobial strategy, owing to its ability to eliminate multidrug-resistant bacteria

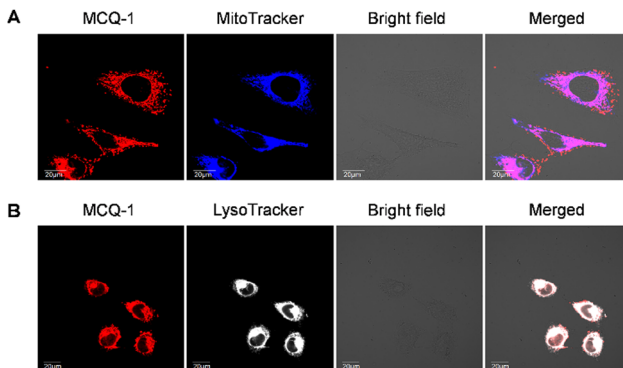


Fig. 4 CLSM images of HeLa cells incubated with **MCQ-1** (5 μM, 30 min) and (A) MitoTracker Blue (0.5 μM, 10 min) or (B) Lysotracker Deep Red (5 μM, 10 min).



through ROS generation under light irradiation, without causing side effects such as the development of antibiotic resistance. Therefore, further tests were performed to evaluate the antibacterial PDT effect of **MCQ-1**. Bacterial experiments were conducted using Gram-positive bacteria, including *S. aureus* and MRSA, as well as Gram-negative bacteria, including *Escherichia coli* O157:H7 (*E. coli*) and extended-spectrum beta-lactamase producing *E. coli* (ESBL *E. coli*).

First, the *in vitro* bacterial fluorescence images of **MCQ-1** were examined using CLSM. When bacteria were treated with **MCQ-1** (1 μ M) for 0, 30, and 60 min, Gram-positive strains (*S. aureus* and MRSA) were rapidly stained, emitting red fluorescence (Fig. 5A and B). Notably, *S. aureus* exhibited immediate staining upon **MCQ-1** treatment. In contrast, Gram-negative strains (*E. coli* and ESBL *E. coli*) showed only weak fluorescence after 30 min of incubation with **MCQ-1**, and only partial staining was observed even after 60 min (Fig. 5C and D). These results indicated that **MCQ-1** exhibits superior activity against Gram-positive bacteria, demonstrating its selective targeting of these strains. This selectivity is likely due to the positive charge of **MCQ-1**, which interacts with the negatively charged thick peptidoglycan layer of Gram-positive bacteria. In contrast, Gram-negative bacteria have a relatively thin peptidoglycan layer and an additional LPS-containing outer membrane, which may hinder the **MCQ-1** binding.

Next, the antibacterial effect of **MCQ-1** was evaluated using LB agar plates. Gram-positive (*S. aureus* and MRSA) and Gram-negative (*E. coli* and ESBL *E. coli*) strains were pretreated with **MCQ-1** at concentrations of 0, 1, 3, 5, and 10 μ M, followed by white LED irradiation (50 mW cm^{-2} , 10 min). As a result, a significantly reduced number of bacterial colonies was observed on the irradiated plates, compared to that on the non-irradiated control plates. Interestingly, as expected from the CLSM experiments, the antibacterial effect was more pronounced on Gram-positive than Gram-negative bacteria (Fig. 6A–D). In Gram-positive bacteria, not only *S. aureus* but

also the antibiotic-resistant MRSA were mostly eliminated at a low **MCQ-1** concentration of 3 μ M, and complete bacterial elimination was observed at 5 μ M. However, some residual *E. coli* and ESBL *E. coli* bacterial colonies remained even after treatment with 10 μ M **MCQ-1**.

Finally, scanning electron microscopy (SEM) was used to examine morphological changes in bacteria following **MCQ-1** treatment with light irradiation. In the case of Gram-positive bacteria, the control group treated only with **MCQ-1** (without light exposure) showed smooth and round bacterial surfaces, without cell membrane damage. In contrast, bacteria treated with **MCQ-1** followed by white LED irradiation (50 mW cm^{-2} , 10 min) exhibited perforated cell membranes, along with shrinkage and deformation. Moreover, both *E. coli* and ESBL *E. coli* maintained intact surfaces under dark conditions, similar to Gram-positive bacteria. A small number of Gram-negative bacteria with damaged membranes were observed upon light irradiation; however, their number was significantly lower compared to that found for the Gram-positive group (Fig. 6E). These results confirm the antibacterial PDT effect of **MCQ-1**, which can selectively kill Gram-positive bacteria under light irradiation.

Experimental

Materials and instruments

^1H NMR and ^{13}C NMR spectra were recorded using AVANCE III 300 (Bruker) and JNM-ECEC500R (JEOL) spectrometers, respectively. The ESI-HRMS measurement was conducted using a Synapt G2-HDMS mass spectrometer at the Korea Basic Science Institute. Fluorescence emission and UV-vis absorption spectra were measured using a FS-2 fluorescence spectrophotometer (Scinco) and a V-770 UV-Visible/NIR Spectrophotometer (JASCO), respectively. CLSM measurements were performed using Olympus Fluoview 3000 and 1200 instruments for colocalization and bacterial imaging, respectively.

Synthesis of **1**³⁰

9-(4-Bromobutyl)-9*H*-carbazole (4 g, 13.23 mmol, 1 eq), morpholine (2.3 g, 26.47 mmol, 2 eq) and dry K_2CO_3 (3.66 g, 2 eq) were stirred together in 50 mL of dry acetonitrile overnight. Then, the reaction mixture was filtered, the solvents were evaporated, and the resulting product was purified by column chromatography using a dichloromethane/methanol mixture (95 : 5, v/v) as the eluent, to obtain compound **1** as a colorless viscous liquid in 98% yield. ^1H NMR (300 MHz, chloroform-*d*) δ 8.12 (d, 2H), 7.51–7.44 (m, 4H), 7.25 (dd, 2H), 4.34 (t, 2H), 3.69 (t, 4H), 2.35 (m, 6H), 1.93 (tt, 2H), 1.58 (tt, 2H).

Synthesis of **2**^{31,32}

A mixture of DMF (1.26 mL, 16.2 mmol, 5 eq) and POCl_3 (1.21 mL, 13.0 mmol, 4 eq) was stirred in an ice bath for 0.5 h, and compound **1** (1 g, 3.24 mmol, 1 eq) dissolved in 1,2-dichloroethane (5 mL) was added to the mixture. After refluxing for 3 h under a nitrogen atmosphere, the reaction

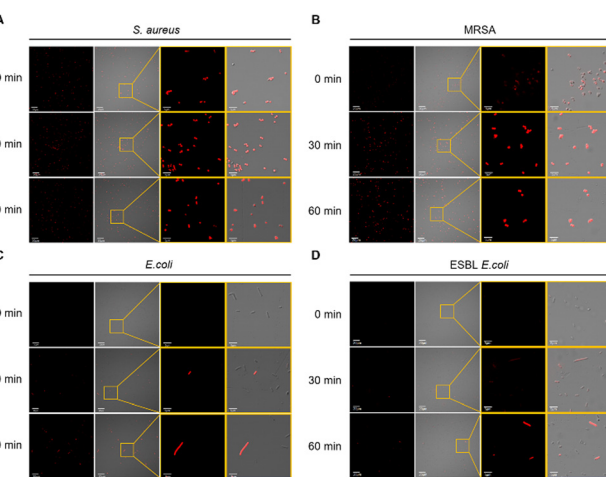


Fig. 5 CLSM images of (A) *S. aureus*, (B) MRSA, (C) *E. coli*, and (D) ESBL *E. coli* treated with **MCQ-1** (1 μ M) with different incubation times (0, 30, and 60 min).



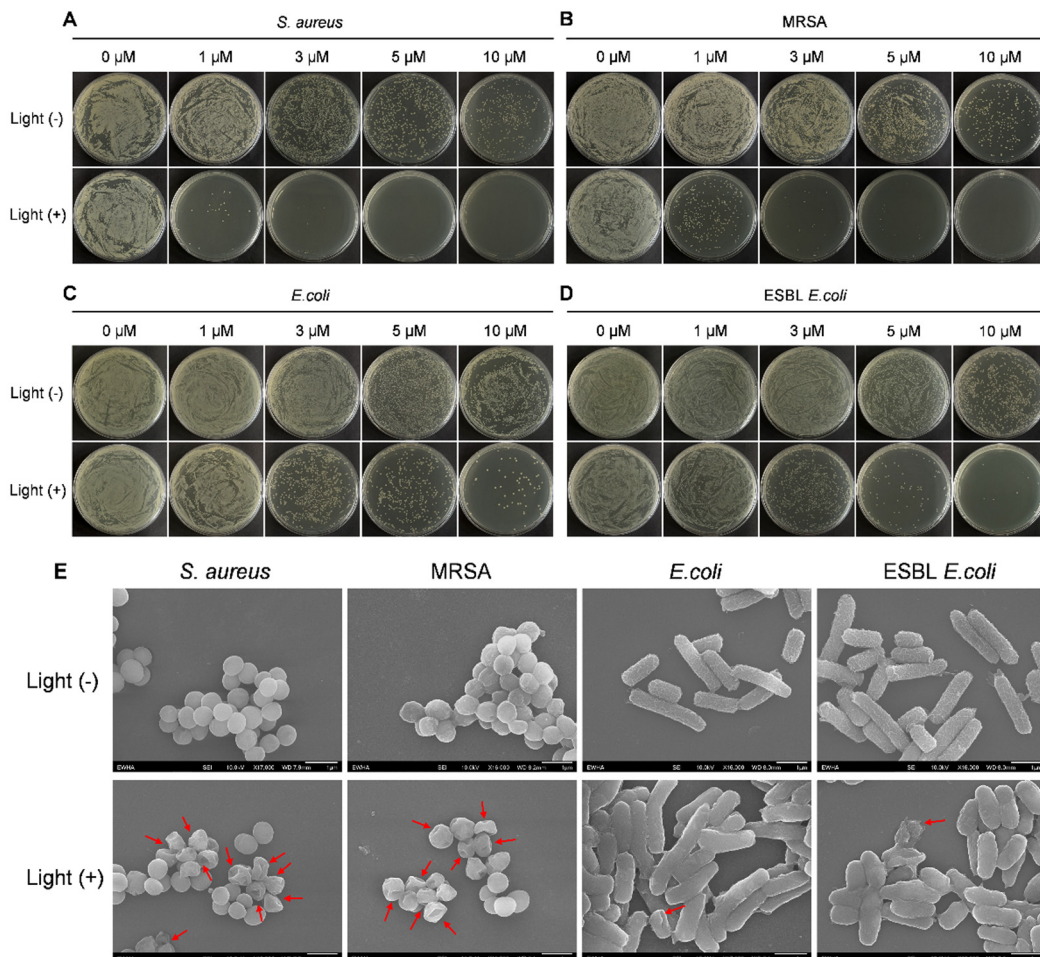


Fig. 6 Photographs of (A) *S. aureus*, (B) MRSA, (C) *E. coli*, and (D) ESBL *E. coli* on LB agar plates treated with various concentrations of **MCQ-1** (0, 1, 3, 5, and 10 μ M) under dark and white LED irradiation (50 mW cm^{-2} , 10 min). (E) SEM images of *S. aureus*, MRSA, *E. coli*, and ESBL *E. coli* treated with **MCQ-1** (3 μ M) under dark and white LED irradiation (50 mW cm^{-2} , 10 min).

mixture was cooled to room temperature, then poured into ice water, quenched with aqueous ammonia, and extracted with dichloromethane. The organic layer was dried over Na_2SO_4 , followed by evaporation and purification by column chromatography using a *n*-hexane/ethyl acetate mixture (2:1, v/v) as the eluent to obtain compound **2** in 93.5% yield. ^1H NMR (300 MHz, chloroform-*d*) δ 10.09 (s, 1H), 8.60 (s, 1H), 8.15 (d, 1H), 8.0 (dd, 1H), 7.57–7.51 (m, 3H), 7.33 (dd, 1H), 4.35 (t, 2H), 3.68 (t, 4H), 2.35 (m, 6H), 1.94 (tt, 2H), 1.57 (tt, 2H).

Synthesis of MCQ-1

Compound **2** (0.286 g, 0.85 mmol, 1 eq) and 1,4-dimethylquinolin-1-ium iodide (0.242 g, 0.85 mmol, 1 eq) were dissolved in 20 mL of anhydrous ethanol. Three drops of piperidine were added as a catalyst. The mixture was refluxed overnight under a nitrogen atmosphere and then cooled to room temperature. After removing the solvent by evaporation, the crude product was purified by column chromatography using a dichloromethane/methanol mixture (30:1, v/v) as the eluent, to obtain **MCQ-1** as a red solid in 50.7% yield. ^1H NMR (300 MHz, DMSO-*d*₆) δ 9.29 (d, 1H), 9.14 (d, 1H), 8.88 (s, 1H), 8.51–8.24 (m, 6H), 8.09 (m, 2H), 7.75 (dd, 2H),

7.54 (t, 1H), 7.31 (t, 1H), 4.51 (s, 3H), 3.52 (4H), 3.34 (2H), 2.27 (6H), 1.83 (2H), 1.49 (2H). ^{13}C NMR (125 MHz, DMSO-*d*₆) δ 153.54, 148.05, 145.39, 142.27, 141.16, 139.32, 135.39, 129.47, 127.20, 126.61, 123.27, 122.70, 122.39, 120.31, 116.69, 115.61, 110.58, 110.56, 44.94, 42.82, 26.66. ESI-HRMS $[\text{C}_{32}\text{H}_{34}\text{N}_3\text{O}]^+$, calcd: 476.2702, found $[\text{M}]^+$: 476.2702.

Spectral analysis

A 1 mM stock solution of **MCQ-1** was prepared by dissolving it in DMSO. The stock solution was then diluted with various solvents (10 μ M, 2 mL), followed by measuring the UV-vis absorption and fluorescence emission spectra. For fluorescence measurements at different pH levels, the **MCQ-1** stock solution (1 mM) was diluted to 10 μ M (2 mL) in ACN/PBS aqueous solution (5:95, v/v). To adjust the pH values for each measurement, NaOH and HCl solutions were used to control the pH of the PBS medium (pH 7.4).

ROS detection

DCFH-DA and HPF were used as fluorescent probes to detect total ROS and hydroxyl radical ($\cdot\text{OH}$) generation, respectively.



A PBS solution (2 mL) containing the detection probe (25 μ M) and **MCQ-1** (10 μ M) was prepared in a cuvette. The cuvette was then exposed to white LED light (50 mW cm^{-2}) for 10 s at a time, and fluorescence was measured immediately after each exposure, continuing for a total of 90 s. Solutions containing only DCFH-DA and HPF were used as controls.

Cell culture

HeLa cell samples, obtained from the Korean Cell Line Bank (Seoul, Korea), were cultured in minimum essential medium (MEM) with 100 U mL^{-1} penicillin, 100 U mL^{-1} streptomycin, and 10% fetal bovine serum (FBS). The cells were incubated at 37 °C in a 5% CO_2 atmosphere.

Cell viability tests

The cultured cells were seeded in a 96-well plate. After overnight incubation, the medium was removed, and the cells were treated with different concentrations of **MCQ-1** (0–20 μ M), followed by incubation for another 24 h. Next, an MTT solution (5 mg mL^{-1}) was added before incubating for an additional 4 h. Formazan crystals were dissolved using 100 μ L of DMSO, and the absorbance was measured using a Spectramax Microwell plate reader.

Colocalization imaging

HeLa cells were seeded in 35-mm glass-bottom dishes at a density of 3×10^5 cells per dish. After overnight incubation, the cells were co-stained with **MCQ-1** (5 μ M) for 30 min and BioTracker 405 Blue Mitochondria Dye (Merck) or Lysotracker Deep Red (Thermo Fisher Scientific) for 10 min. The dishes were then washed with DPBS, and confocal fluorescence images were obtained using an Olympus Fluoview 3000 microscope.

Bacterial culture

Antibacterial tests were conducted using Gram-positive bacteria such as *S. aureus* (25923) and MRSA (CCRAM 3696), as well as Gram-negative bacteria including *E. coli* (ATCC 43894) and ESBL *E. coli* (ATCC BAA-198). The bacteria were first grown on LB agar plates overnight; then, 3–5 colonies from each plate were transferred to 4 mL of LB broth culture and incubated for several hours at 37 °C with shaking at 200 rpm. The optical density (OD) of the bacterial solution at 600 nm was adjusted to 1.0 to standardize the bacterial concentration, ensuring consistent values across the experiments.

Confocal fluorescence imaging

1 mL of bacterial culture was centrifuged at 5000 rpm to obtain a bacterial pellet, which was then washed three times with PBS. The pellet was treated with **MCQ-1** (1 μ M) in PBS (1 mL) and incubated for 0, 30, and 60 min, respectively. The bacterial solution was centrifuged again, and the pellet was resuspended in an appropriate amount of PBS. Finally, the suspension was placed on a glass microscope slide, and fluorescence images were obtained using an Olympus Fluoview 1200 microscope.

Antibacterial PDT effects

For antibacterial experiments, 1 mL of bacterial culture adjusted to an OD of 1.0 was centrifuged at 5000 rpm to obtain a bacterial pellet. The latter was washed three times with PBS, followed by the addition of 1 mL of PBS to prepare the bacterial stock solution. Next, 100 μ L of the bacterial stock solution was mixed with various concentrations of **MCQ-1** (0, 1, 3, 5, and 10 μ M) in 1 mL of PBS solution, and the resulting mixture was incubated at 37 °C with shaking at 200 rpm for 2 h. After incubation, 200 μ L of each sample was exposed to white LED light (50 mW cm^{-2}) for 10 min. The irradiated solutions were then diluted 10 times with PBS, and 200 μ L of each diluted solution was spread on LB agar plates. Finally, the plates were incubated at 37 °C overnight.

SEM detection

The bacterial culture was centrifuged at 5000 rpm, and the bacterial precipitate was washed three times with PBS. The obtained product was treated with **MCQ-1** (3 μ M) in PBS (1 mL) and incubated for 2 h. Each sample was irradiated with white LED light (50 mW cm^{-2}) for 10 min, then centrifuged and fixed with 2% paraformaldehyde, and sequentially dehydrated using ethanol solutions of increasing concentrations (30%, 50%, 75%, 85%, 95%, and 100%). Finally, the dehydrated bacterial samples, placed on a silicon wafer, were allowed to dry and then examined using SEM.

Theoretical methods

All calculations were performed with the ORCA 6.0.1 software package³⁵ at the CAM-B3LYP/TZVP level of theory.³⁶ Solvent effects were included using the SMD solvation model, with water as the solvent.³⁷ The DFT-D3 dispersion correction was applied throughout the calculations. Electron-hole analysis was performed using the Multiwfn 3.8 package.³⁸

Conclusions

Photoactivated fluorescent probes capable of inducing lysosomal dysfunction and mitochondrial damage *in situ* are highly desirable, owing to advantages such as light-controlled imaging with high spatial resolution and the enhanced therapeutic effects of dual-organelle disruption. In this study, we developed and characterized a novel dual-targeting type I PS, **MCQ-1**, capable of localizing both mitochondria and lysosomes in cancer cells. This compound exhibited favorable photophysical properties, including a large Stokes shift and strong red fluorescence, enabling effective cellular imaging. Moreover, **MCQ-1** showed a strong pH-dependent fluorescence behavior, with enhanced emission in acidic environments, and maintained a sufficiently strong signal under physiological conditions, highlighting its applicability in biological systems.

Upon white light irradiation, **MCQ-1** efficiently generated ROS, including hydroxyl radicals ($\cdot\text{OH}$), *via* a type I photodynamic mechanism. Confocal imaging confirmed its dual-targeting capability, with high colocalization to mitochondria and lysosomes. Importantly, **MCQ-1** showed low cytotoxicity in



the dark but high phototoxicity under light exposure, highlighting its potential as a safe and effective PDT agent.

Furthermore, **MCQ-1** exhibited selective antibacterial activity against Gram-positive bacteria, including MRSA, through a light-triggered PDT process. This compound also enabled rapid and selective staining of Gram-positive bacteria and induced significant morphological damage upon irradiation. In contrast, Gram-negative bacteria showed limited susceptibility to **MCQ-1**, indicating that the observed specificity is likely driven by bacterial cell wall composition.

Taken together, these results demonstrate that **MCQ-1** is a promising dual-functional photosensitizer that combines organelle-targeted cancer therapy and selective antimicrobial activity. Its dual-targeting ability, efficient ROS generation, and biocompatibility make it a valuable candidate for further applications in both oncology and infectious disease treatment.

Author contributions

Chaewoon Cho: synthesis, investigation, and writing – original draft. K. M. K. Swamy: conceptualization and synthesis. Bingqing Sun: theoretical calculations and writing – review and editing. Gyoungmi Kim: cell culture and confocal fluorescence imaging. Lei Liu: theoretical calculations and writing – review and editing. Won Jun Jang: writing – review and editing. Juyoung Yoon: conceptualization and writing – original draft and editing.

Conflicts of interest

There are no conflicts to declare.

Data availability

The data supporting this article have been included as part of the ESI.†

Acknowledgements

This work was supported by the National Research Foundation (NRF), funded by the Korean government (MSIT) (RS-2023-00217701). K. M. K. Swamy thanks the Brain Pool program, funded by the Ministry of Science and ICT through the National Research Foundation of Korea (RS-2023-00304224). This research was also supported by the Natural Science Foundation of the Anhui Higher Education Institutions of China (Grant No. gxgwx2021037 and gxgwx2022027) and the Foundation of the Anhui Science and Technology University (Grant No. 2021zrzd15). NMR measurements were performed using the 300 MHz spectrometer at the National Research Facilities and Equipment Center (NanoBioEnergy Materials Center) of Ewha Womans University.

Notes and references

1 X.-X. Lu, C. Xue, J.-H. Dong, Y.-Z. Zhang and F. Gao, *J. Mater. Chem. B*, 2024, **12**, 3209–3225.

- 2 X. Lyu, J. Yu, L. Zhang, Y. Zhao, Z. Qiu, Y. Chen, Z. Zhao and B. Z. Tang, *J. Mater. Chem. B*, 2023, **11**, 5953–5975.
- 3 Y.-Y. Zhao, H. Kim, V.-N. Nguyen, S. Jang, W. J. Jang and J. Yoon, *Coord. Chem. Rev.*, 2024, **501**, 215560.
- 4 T. Xiong, Y. Chen, Q. Peng, X. Zhou, M. Li, S. Lu, X. Chen, J. Fan, L. Wang and X. Peng, *Adv. Mater.*, 2025, **37**, 2410992.
- 5 Y.-Y. Zhao, X. Zhang, Y. Xu, Z. Chen, B. Hwang, H. Kim, H. Liu, X. Li and J. Yoon, *Angew. Chem., Int. Ed.*, 2024, **63**, e202411514.
- 6 B. Lu, L. Wang, H. Tang and D. Cao, *J. Mater. Chem. B*, 2023, **11**, 4600–4618.
- 7 S. Zeng, J. Wang, H. Kang, H. Li, X. Peng and J. Yoon, *Angew. Chem., Int. Ed.*, 2025, **64**, e202417899.
- 8 R. Wang, X. Li and J. Yoon, *ACS Appl. Mater. Interfaces*, 2021, **13**, 19543–19571.
- 9 N. Sun, R. J. Youle and T. Finkel, *Mol. Cell*, 2016, **61**, 654–666.
- 10 H. Li, H. Kim, C. Zhang, S. Zeng, Q. Chen, L. Jia, J. Wang, X. Peng and J. Yoon, *Coord. Chem. Rev.*, 2022, **473**, 214818.
- 11 Q. Ding, X. Wang, Y. Luo, X. Leng, X. Li, M. Gu and J. S. Kim, *Coord. Chem. Rev.*, 2024, **508**, 215772.
- 12 E. R. H. Walter, P. K.-K. Leung, L. C.-C. Lee, K. K.-W. Lo and N. J. Long, *J. Mater. Chem. B*, 2024, **12**, 10409–10415.
- 13 H. Li, Y. Lu, J. Chung, J. Han, H. Kim, Q. Yao, G. Kim, X. Wu, S. Long, X. Peng and J. Yoon, *Chem. Sci.*, 2021, **12**, 10522–10531.
- 14 C. Kim, H. Kim, J. Jo, S. Kim, A. M. Bongo, H.-J. Kim and J. Yang, *ACS Appl. Bio Mater.*, 2024, **7**, 8294–8304.
- 15 W. Li, S. Yin, Y. Shen, H. Li, L. Yuan and X. Zhang, *J. Am. Chem. Soc.*, 2023, **145**, 3736–3747.
- 16 Z. Zhou, S. Li, X. Ding, K. Zhang, J. Zhou and X. Zhou, *ACS Appl. Bio Mater.*, 2025, **8**, 3464–3472.
- 17 C. Su, P. Xing, J. Zhang, X. Ma, X. Wu, M. Zhu, X. Zhang, H. Du, Y. Bian and J. Jiang, *Dyes Pigm.*, 2024, **222**, 111861.
- 18 H. Wu, S. Lee, H. Kim, S. Hong, T. Kim, S. Yeo, W. K. Lee and I. Yoon, *Dyes Pigm.*, 2024, **224**, 112039.
- 19 K. Xue, P. Zhang, Y. Zhao, S. Sun, Y. Li, J. Liang and Z. Qi, *Dyes Pigm.*, 2023, **217**, 111442.
- 20 Z. Liu, Z. Tang, Y. Yin, M. Wan, J. Zhan and L. Ren, *Adv. Healthcare Mater.*, 2025, 2403954.
- 21 X. Wen, Z. Shi, Y. Huang and Z. Fan, *New J. Chem.*, 2024, **48**, 19136–19143.
- 22 F. F. Li, J. G. Collins and F. R. Keene, *Chem. Soc. Rev.*, 2015, **44**, 2529–2542.
- 23 B. Hu, C. Owh, P. L. Chee, W. R. Leow, X. Liu, Y. L. Wu, P. Guo, X. J. Loh and X. Chen, *Chem. Soc. Rev.*, 2018, **47**, 6917–6929.
- 24 P. C. Ray, S. A. Khan, A. K. Singh, D. Senapati and Z. Fan, *Chem. Soc. Rev.*, 2012, **41**, 3193–3209.
- 25 H. Kim, Y. R. Lee, H. Jeong, J. Lee, X. Wu, H. Li and J. Yoon, *Smart Molecules*, 2023, **1**, e20220010.
- 26 W. Zhou, Q. Qiao, Y. Tao, C. Duan, J. Li, X. Fang, N. Xu, J. Chen, W. Liu, L. Miao and Z. Xu, *Sens. Actuators, B*, 2024, **410**, 135691.
- 27 J. H. Liu, X. L. Chen, H. M. Yang, Y. R. Yin, A. Kurniawan and Ch. H. Zhou, *J. Mater. Chem. B*, 2024, **12**, 6874–6885.
- 28 X. Wu, M. Yang, J. S. Kim, R. Wang, G. Kim, J. Ha, H. Kim, Y. Cho, K. T. Nam and J. Yoon, *Angew. Chem., Int. Ed.*, 2022, **61**, e202200808.



29 Ferdinandus, C. Joo, D. Kai and C.-L. Ken Lee, *J. Mater. Chem. B*, 2023, **11**, 5748–5751.

30 B. Maji, K. Kumar, M. Kaulage, K. Muniyappa and S. Bhattacharya, *J. Med. Chem.*, 2014, **57**, 6973–6988.

31 J. Luo, G. Song, X. Xing, S. Shen, Y. Ge and X. Cao, *New J. Chem.*, 2017, **41**, 3986–3990.

32 Z. Fang, F. Pei, Z. Chao, L. Hui, Q. Ying and W. Xiang, *Indian J. Chem.*, 2016, **55B**(6), 713–717.

33 Q. Wan, R. Zhang, Z. Zhuang, Y. Li, Y. Huang, Z. Wang, W. Zhang, J. Hou and B. Z. Tang, *Adv. Funct. Mater.*, 2020, **30**, 2002057.

34 Z. Liu, Q. Wang, W. Qiu, Y. Lyu, Z. Zhu, X. Zhao and W. H. Zhu, *Chem. Sci.*, 2022, **13**, 3599–3608.

35 F. Neese, The ORCA program system, *WIREs Comput. Mol. Sci.*, 2012, **2**, 73–78.

36 A. V. Marenich, C. J. Cramer and D. G. Truhlar, *J. Phys. Chem. B*, 2009, **113**, 6378–6396.

37 S. Grimme, J. Antony, S. Ehrlich and H. Krieg, *J. Chem. Phys.*, 2010, **132**, 154104.

38 T. Lu and W. F. Chen, *J. Comput. Chem.*, 2012, **33**, 580–592.

39 X. Kang, Z. Du, S. Yang, M. Liang, Q. Liu and J. Qi, *Smart Molecules*, 2024, **2**, e20240033.

